Slipping domains in water-lubricated microsystems for improved load support

Daniele Savio[a,*], Kerstin Falk[a], Michael Moseler[a,b]

[a]Microtribology Center μTC, Fraunhofer Institute for Mechanics of Materials IWM, Whlerstr. 11, D-79108 Freiburg, Germany
[b]Albert-Ludwigs-University of Freiburg, Herrmann-Herder-Str. 3, D-79104 Freiburg, Germany

Abstract

This work discusses the use of slipping domains to improve load support in water-lubricated microsystems through a multi-scale approach. A semi-analytical continuum formulation is developed to calculate changes in pressure distribution for a line contact with added slip. It is found that the slipping region maximizing hydrodynamic lift should favor inlet flow, but not be located at the contact outlet. Estimations for its positioning are provided. Slip on flat surfaces gives the largest gains in load support and friction reduction, but moderate improvements are also possible on circular geometries featuring high convergence ratios. Finally, Molecular Dynamics simulations are employed to quantify slip on hydrophobic surfaces. Among the considered topologies, graphene is an excellent candidate to generate slip in water-lubricated microsystems.

Keywords: Wall slip, hydrophobicity, microsystems, nanometer-thin lubricant films, hydrodynamic flow, Molecular Dynamics

1. Introduction

In the past decades miniaturization of technology has been applied to mechanical systems, biomedical applications, "lab-on-a-chip" analysis tools, sensors, and data storage. This trend has given rise to a new class of devices called Micro-Electro-Mechanical System (MEMS). Yet, from a tribological point of view, the usual problematic of friction and wear reduction is still present in this microscopic framework. For instance, stiction remains a critical issue [1]: due to large surface tension of capillary bridges and high adhesion, the contacting surfaces can stick together under operation. This phenomenon may lead to component wear and failure. A possible solution is to employ low surface energy coatings to reduce capillary forces, direct chemical bonding and electrostatic interactions between walls [2]. Such modification of the surface chemistry can for instance be achieved through deposition of hydrocarbon or fluorocarbon chlorosilane-based self-assembled monolayers (SAMs) [3, 4]. Additionally, one could reduce stiction by favoring hydrodynamic lubrication in the contact regions by the means of operating fluids already present in the system. An example is water, which is often found between MEMS surfaces due to condensation [1].

Interestingly, low surface energy coatings could be adapted to improve both direct surface contact and hydrodynamic lubrication. The underlying idea is that changes in surface chemistry may result in wall slip of the lubricant. This phenomenon is a velocity jump at a surface-fluid interface which contradicts the usual no-slip boundary condition in continuum fluid dynamics [5]. Its occurrence influences the lubricant dynamics across the film thickness, which can be exploited to tailor and enhance fluid transport in microfluidic applications [6, 7]. In tribological devices wall slip can be used to improve load support and reduce friction in the hydrodynamic regime, if applied only to a part of the surfaces. Possible benefits have been investigated numerically at the continuum scale through a modified Reynolds equation including slip boundaries [8, 9, 10, 11, 12, 13]. These studies have revealed that the enhancement of hydrodynamic lift is related to a modified pressure generation along the whole contact length, but can also be impacted by the occurrence of cavitation [14]. Moreover, load support was significantly increased when applying a slipping domain to parallel walls, compared to the optimum plane slider without slip [12]. Thus, most studies on heterogeneous

*Corresponding author
Email address: daniele.savio@iwm.fraunhofer.de (Daniele Savio)

slip in macroscopic systems have generally focused on low pitch angles of the surfaces and a planar contact geometry. Yet, severe surface tilting may occur in MEMS due to mounting on flexible supports and the presence of high lateral forces, leading to highly sloped walls. In addition, more complex contact geometries can be found, like for instance rounded or rough surfaces. In order to fully exploit the addition of slip in microsystems, such configurations should be analyzed further using continuum methods.

Another issue is determining which surface chemistry should be employed to achieve the desired slip values for a given lubricant. For this purpose continuum methods cannot be used, since slip is an imposed boundary condition. In addition, the analysis should be performed for nanometer-thin lubricant films, which are expected in MEMS due to the small contact dimensions, and low viscosity of the operating fluid used for lubrication. Experimental techniques require flow measurements [15] or photobleached-fluorescence imaging [16, 17] in thin gaps. Alternatively, atomistic simulations based on the Molecular Dynamics (MD) method can be applied to nanometer-thin fluid films expected in microsystems. Continuous development of potentials for an accurate description of fluid behavior [18] and the surface-fluid interactions [19] offer interesting perspectives for MD a quantitative tool for slip prediction under realistic contact conditions. Considerable amount of work has been performed for different shear rates [20, 21], pressures [22], as well as for several confined lubricants and surfaces [23, 24, 25]. The occurrence of wall slip has been linked to weak surface-fluid interactions and incommensurability [7, 25], which can also lead to hydrophobic and oleophobic behavior with high contact angles for droplets on the walls [26]. Finally, a direct incorporation of slip values from MD into continuum models was performed in a recently developed multiscale framework for highly loaded lubricated contacts [22, 27]. The approach was validated for a heterogeneous slip system and nanometer-thin films through a direct comparison between large scale MD simulations and a simple hydrodynamic model [28].

In this work, this multi-scale approach will be applied to a water-lubricated microsystem in the hydrodynamic regime. The goal is to assess possible improvements in load support and friction by adding a slipping patch, with particular attention to slanted and nonplanar contact geometries. For this purpose, a semi-analytical solution of the hydrodynamic problem will be proposed, which requires only the calculation of integrals. The positioning of the slipping patch maximizing load support will be analyzed for several surface slopes and contact geometries. Moreover, simple expressions for the estimation of the optimum slipping region will be derived. Then, theoretical gains in hydrodynamic lift and friction at the contact length scale will be evaluated. Finally, Molecular Dynamics simulations will be employed to quantify slip of water on different hydrophobic coatings, followed by a discussion on the possible scopes of application for improved contact performance in MEMS.

2. Continuum analysis of slip on slanted surfaces

Our work on slipping domains in MEMS begins at the scale of the contact length, i.e. some μm to mm, by the means of a continuum approach. Several contact geometries are analyzed in the hydrodynamic lubrication regime. Our first goal is to discuss the ideal positioning of the slipping patch which maximizes hydrodynamic lift as a function of wall slip and the surface slope. The second objective is to assess theoretical improvements in load support and friction in the hydrodynamic lubrication regime. Compared to existing works on planar sliders with parallel walls or low pitch angles, we will also focus on highly slanted surfaces and a cylindrical contact geometry. A study on these configurations is motivated by the difficulty to control exactly the surface inclination in microsystems. For instance, tilting can occur under operation if the surfaces are mounted on flexible supports and in presence of high lateral forces. Additionally, it is crucial to assess the effect of slip on rounded, e.g. cylindrical tips compared to ideally flat surfaces.

In the hydrodynamic continuum model, a convergent gap of length L is thus considered, with inlet and outlet film thicknesses h_1 and h_2, respectively. The lower surface moves with a velocity U along the x-direction and entrains the fluid inside the contact. The two convergent shapes shown in Fig. 1a-b are chosen. The first is a plane slider, with a gap $h(x)$ between surfaces:

$$h(x) = h_2\left[1 + (1 - x/L)(a - 1)\right] \tag{1}$$

where $a = h_1/h_2$ is the convergence ratio between inlet and outlet film thickness. The second is a half-cylinder with:

$$h(x) = h_2 - \sqrt{R^2 - (x - L)^2} + R \quad \text{with} \quad R = \frac{L}{\sin\left[\pi - 2\arctan(\frac{L}{h_2(a-1)})\right]} \tag{2}$$

where the value of the ratio h_2/L is fixed to 10^{-3}, a typical value for lubrication problems.

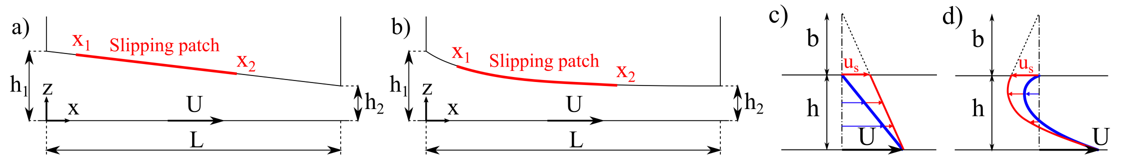

Figure 1: Schematic representation of the planar (a) and circular (b) contact geometries. c-d) Slip length b on the upper surface and its effect on Couette and Couette-Poiseuille flow. u_s is the resulting slip velocity at the wall. The velocity profiles without (blue) and with slip (red) are also shown.

A slipping patch is placed between positions x_1 and x_2 on the upper surface (Fig. 1a-b). Wall slip is quantified by a Navier slip length $b = -u_s / \frac{\partial u}{\partial z}|_{z=h}$, where u_s is the slip velocity and $\frac{\partial u}{\partial z}|_{z=h}$ the gradient in fluid velocity at the upper wall. This slip model is justified by the Molecular Dynamics results from Section 3. A graphical representation of this boundary condition is given in Fig. 1c-d. Over the whole contact length, the slip condition writes:

$$b(x) = \begin{cases} b = \text{constant}, & \text{if} x \in [x_1, x_2]\,. \\ 0, & \text{otherwise.} \end{cases} \tag{3}$$

The choice of a single slipping domain is motivated by potential applications in microsystems. Here, slip may be achieved through chemical modifications of the surfaces, like nonwetting coatings. At the micro- and nanoscales it can prove easier to apply such materials to a large part of the walls, compared to arrays of small patches which are usually proposed for the texturing of larger devices.

2.1. Continuum equations

The hydrodynamic model for the contact geometries in Figure 1a-b is based upon the classical assumptions of the lubrication theory, i.e. the thin film approximation, negligible inertia, constant fluid viscosity η and density ρ. Integration of the simplified Navier-Stokes equations with a standard no-slip boundary condition for the lower moving surface, and a Navier slip length $b(x)$ on the immobile upper surface, gives the velocity profile in shearing direction across the gap width:

$$u(x,z) = \frac{1}{2\eta}\frac{\partial P}{\partial x}\left[z^2 - zh(x)\left(\frac{h(x)+2b(x)}{h(x)+b(x)}\right)\right] + U\left[1 - \frac{z}{b(x)+h(x)}\right] \tag{4}$$

The resulting slipping velocity and gradient on the upper wall are:

$$\begin{aligned} u(h,x) &= \frac{h(x)^2}{2\eta}\frac{\partial P}{\partial x}\left(-\frac{b(x)}{h(x)+b(x)}\right) + U\left[\frac{b(x)}{b(x)+h(x)}\right] \\ \left.\frac{\partial u}{\partial z}\right|_{x,z=h} &= -\frac{h(x)^2}{2\eta(b(x)+h(x))}\frac{\partial P}{\partial x} - \frac{U}{b(x)+h(x)} \end{aligned} \tag{5}$$

The pressure distribution $P(x)$ is crucial for determining load support and friction in the hydrodynamic regime. In the present work we propose a solution for the steady-state line contact problem with slip, requiring only the numerical evaluation of integrals. We assume that the pressure distribution $P_0(x)$ for the no-slip problem, denoted from now on with index $_0$, is known.

The new pressure distribution $P(x)$ is linked to changes the lubricant flow introduced by the slipping patch. The volumetric flow rates are given by:

$$\Phi = \int_0^h u(x,z)dz = \frac{1}{12\eta}\frac{\partial P}{\partial x}\left(-h(x)^3\left[1 + \frac{3b(x)}{b(x)+h(x)}\right]\right) + \frac{Uh(x)}{2}\left(1 + \frac{b(x)}{b(x)+h(x)}\right) \tag{6}$$

and

$$\Phi_0 = \frac{-h(x)^3}{12\eta}\frac{\partial P_0}{\partial x} + \frac{Uh(x)}{2} \tag{7}$$

for the slip and no-slip cases respectively. The flow rate change $\Delta\Phi = \Phi - \Phi_0$ is:

$$\Delta\Phi = \frac{1}{12\eta}\frac{\partial P}{\partial x}\left(-h(x)^3\left[1+\frac{3b(x)}{b(x)+h(x)}\right]\right)+\frac{h(x)^3}{12\eta}\frac{\partial P_0}{\partial x}+\frac{Uh(x)}{2}\left(\frac{b(x)}{b(x)+h(x)}\right) \tag{8}$$

Note that in the previous equations the slip length $b(x)$ can be dependent on the spatial coordinate x along the shearing direction. On the other hand, Φ, Φ_0 and thus $\Delta\Phi$ must remain constant along the contact length due to mass conservation of the lubricant from the inlet to the outlet. Eq. 8 is rewritten to single out the pressure gradient $\partial P/\partial x$ and then integrated along the contact length:

$$\int_0^L \frac{\partial P}{\partial x}dx = \int_0^L\left[\frac{\partial P_0}{\partial x}\left(\frac{b(x)+h(x)}{4b(x)+h(x)}\right)+\frac{6\eta U}{h(x)^2}\left(\frac{b(x)}{4b(x)+h(x)}\right)\right]dx - 12\eta\Delta\Phi\int_0^L\left(\frac{1}{h(x)^3}\frac{b(x)+h(x)}{4b(x)+h(x)}\right)dx = 0 \tag{9}$$

Due to the imposed ambient pressure at contact inlet and outlet ($P(0) = P_0(0) = P(L) = P_0(L) = P_{\text{amb.}}$), Eq. 9 is nil. Hence, the flow change $\Delta\Phi$ writes:

$$\Delta\Phi = \frac{\int_0^L\left[\frac{\partial P_0}{\partial x}\left(\frac{b(x)+h(x)}{4b(x)+h(x)}\right)+\frac{6\eta U}{h(x)^2}\left(\frac{b(x)}{4b(x)+h(x)}\right)\right]dx}{12\eta\int_0^L\left[\frac{b(x)+h(x)}{h(x)^3(4b(x)+h(x))}\right]dx} \tag{10}$$

Finally, the pressure distribution $P(x)$ with slipping domain is given by:

$$P(x) = \int_0^x\left[\frac{\partial P_0}{\partial x}\left(\frac{b(x)+h(x)}{4b(x)+h(x)}\right)+\frac{6\eta U}{h(x)^2}\left(\frac{b(x)}{4b(x)+h(x)}\right)\right]dx - 12\eta\Delta\Phi\int_0^x\left(\frac{1}{h(x)^3}\frac{b(x)+h(x)}{4b(x)+h(x)}\right)dx \tag{11}$$

Despite their complex form, Eqs. 10-11 can easily be evaluated numerically.

Additionally, the condition $P(x) \geq 0$ (Half-Sommerfeld cavitation model) prevents negative pressures in 11. Note that, although this phenomenon can appear for slip on parallel surfaces [14] or low pitch angles, it does not occur for very slanted walls which are the focus of this work. In addition to this simple cavitation model, another limitation of the proposed approach is the extension to 3-dimensional problems, which could prove difficult due to fluid flow at the sides of the contact. Despite these restrictions, the proposed method constitutes a fast computation tool for the pressure distribution in line contacts with slip for virtually any convergent shape $h(x)$. Moreover, the slip length $b(x)$ is not limited to a constant value, and can follow a complex evolution in the shearing direction x. This opens up promising perspectives for the investigation of wettability changes along the contact length, like in the case of gradient surfaces.

The newly calculated pressure distribution is then used to evaluate theoretical improvements in contact performance generated by the slipping patch. A key parameter is the load support generated in the pressurized domain, which should be maximized to enhance surface separation and reduce wear. This quantity, called respectively $W1$ and $W1_0$ for the slip- and no-slip cases, is given by:

$$W1 = \int_0^L P(x)dx \quad ; \quad W1_0 = \int_0^L P_0(x)dx \tag{12}$$

The relative increase in line load support due to slip is then $\frac{W1-W1_0}{W1_0}$. Another possible improvement in contact performance involves a reduction in viscous friction. The tangential friction force on the lower moving surface is calculated as:

$$F_T = \int_0^L \eta\left.\frac{\partial u}{\partial z}\right|_{z=0}dx = \int_0^L\left[-h\frac{2b+h}{2(b+h)}\frac{\partial P}{\partial x}-\frac{\eta U}{b+h}\right]dx \quad ; \quad F_{T0} = \int_0^L\left[-\frac{h}{2}\frac{\partial P_0}{\partial x}-\frac{\eta U}{h}\right]dx \tag{13}$$

where the resulting relative change in friction due to the slipping patch is given by $\frac{F_T-F_{T0}}{F_{T0}}$.

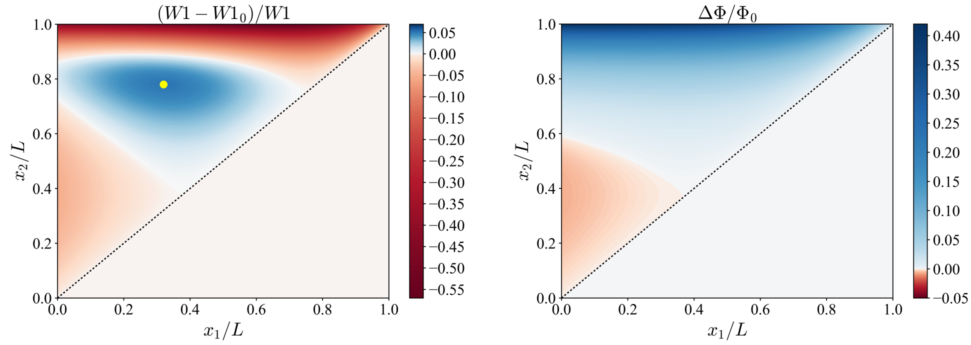

Figure 2: a) Relative gain in load carrying capacity, and b) flow rate modification as a function of the limits x_1 and x_2 of the slipping patch. Note that the condition $x_1 < x_2$ applies. Blue domains mark higher load support and higher flow rate compared to the no-slip solution, red a reduction in these quantities. The x_1, x_2 values giving maximum hydrodynamic lift are marked by the yellow dot. These results were obtained for a configuration with $h1_/h2 = 3$ and a slip length $b/h_2 = 1.0$.

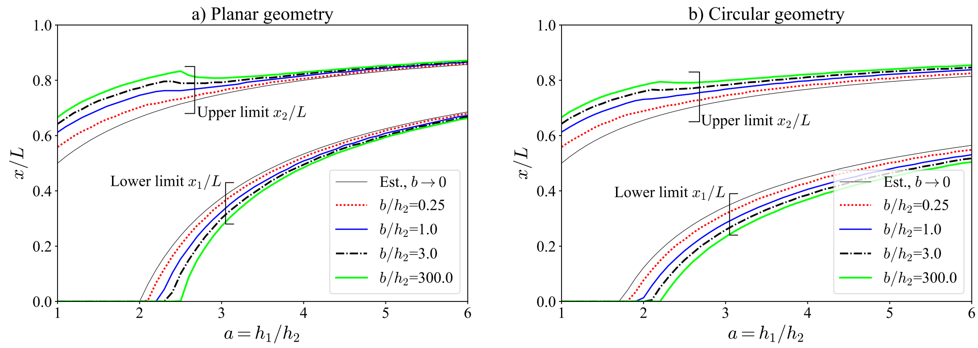

Figure 3: Limits x_1 and x_2 of the slipping patch maximizing load support for different slip lengths b and convergence ratios a between inlet and outlet film thickness. The black line shows the $[x_1, x_2]$ values estimated for vanishing slip length in Eqs. 14-15.

2.2. *Positioning of the patch for maximum load support*

An extensive parametric study is carried out to asses the location of the slipping domain which maximizes hydrodynamic lift, as well as resulting gains in load support and friction reduction. Calculations are performed for the two geometries of Figure 1, several values of the slip length ($b/h_2 = 10^{-4} - 300$), and convergence ratios a ranging from 1.0 (parallel surfaces) to 6.0. For each single contact configuration, 600x600 locations between the contact inlet ($x = 0$) and outlet ($x = L$) are considered for the bounds x_1, x_2 of the slipping patch. The optimum positioning corresponds to the $[x_1, x_2]$ pair maximizing load support. An example of this analysis for a planar slider with $a = 3.0$ and a slip length of $b = h_2$ is represented in Figure 2a, where the best slipping domain is marked by the yellow dot.

Figure 3 shows the limits of the slipping domain which maximize load support as a function of the convergence ratio between inlet and outlet film thickness. Very similar trends are obtained for the planar and the circular slider geometries. First, the chosen slip length has only a moderate impact on the values of x_1 and x_2: varying b by several orders of magnitude results in an average broadening of the optimum slipping domain by approximately 30%. Moreover, Figure 2a indicates that small variations in the location of $[x_1, x_2]$ from the optimum values do not impact significantly the improvement in load support.

On the other hand, a peculiar dependence of the best positioning of the slipping patch on the convergence ratio is found in both the planar and circular cases. For parallel walls and low surface slopes the optimum slipping domain begins at the contact inlet ($x_1 = 0$) and extends approximately to the middle of the contact, in accordance with previous numerical studies [12]. In clear contrast with this picture are the results for higher convergence ratios $a \gtrsim 2$: here the slipping domain should not be placed in the inlet region and instead shifted towards the middle of the convergent. Better understanding of this phenomenon can prove helpful in unlocking performance gains from wall slip at high surface slopes. In the following, an estimation of the limits $[x_{1,est.}, x_{2,est.}]$ of the domain maximizing load support is proposed based on simple flow considerations.

Fig. 2 provides further insight on the underlying physics. In Fig. 2a three possible placements of the slipping patch result in largely different impacts on load support: the contact center, which is beneficial, and the inlet and outlet regions, which are detrimental compared to the no-slip case. Fig. 2b shows the corresponding modification in volumetric flow rate $\Delta\Phi$. The reduction in load support caused by slip at the contact inlet appears to be linked with a reduction in lubricant flow ($\Delta\Phi < 0$): effectively, slip in this region prevents the fluid from entering the contact and generating lift. If the inlet region presents reverse flow (e.g. at high surfaces slopes), the condition $\frac{\partial u}{\partial z}|_{z=h} > 0$ applies in proximity of the upper wall. According to the geometrical definition of the slip length in Section 2.1, adding slip here results in a negative velocity $u_s = -b\frac{\partial u}{\partial z}|_{z=h}$ at the upper surface, thereby reducing the flow rate. This modification of the fluid velocity profile is schematically represented in Fig. 1d. The slipping patch should instead be located in a domain without such reverse flow to improve contact performance. Its limit can be estimated as the abscissa $x_{1,\text{est.}}$ where both the velocity gradient at the upper surface and the slip velocity (Eq. 5) are zero. At vanishing slip length $b \to 0$, for which the pressure $P(x) \simeq P_0(x)$ equals the one of the no-slip case, $x_{1,\text{est.}}$ must satisfy the following equation:

$$\frac{h(x_{1,\text{est.}})}{2\eta} \frac{\partial P_0}{\partial x}\bigg|_{x_{1,\text{est.}}} - \frac{U}{h(x_{1,\text{est.}})} = 0 \tag{14}$$

At low surface slopes, where no reverse flow occurs at the contact inlet, the estimated value is $x_{1,\text{est.}} = 0$ in accordance with the results from the parametric study. Nonetheless, the aforementioned increase in fluid flow rate compared to the no-slip case is not sufficient to improve performance. Fig. 2 shows that slip at the contact exit leads to maximum $\Delta\Phi$, but also to severe losses in load support. A likely explanation is that slip at the outlet causes the fluid to leave rapidly the contact, and impedes the generation of hydrodynamic lift on the walls.

Further insight on this phenomenon is provided by Appendix A, which analyzes how an extension of the slipping domain towards the contact outlet impacts hydrodynamic lift. It is revealed that the modification in load support scales with the flow rate change due to the extension, and an additional contribution $W_h(x_2)$ dependent on the convergent geometry $h(x)$ and the upper bound x_2 of the slipping patch. W_h is positive for x_2 at contact inlet and center: here, extending the slipping domain improves hydrodynamic lift. Conversely, W_h is negative for x_2 near the outlet: further extension of the slipping domain reduces load support despite an increase in flow rate, as shown in Fig. 2. Finally, the crossover point where $W_h = 0$ marks the location $x_{2,est.}$ beyond which the slipping region should not be extended. For vanishing slip length $b \to 0$, this estimation of the upper limit of the slipping is:

$$x_{2,est.} = L - \frac{\int_0^L \left[\int_0^\zeta h(x)^{-3} dx\right] d\zeta}{\int_0^L h(x)^{-3} dx} \tag{15}$$

In summary, load support can be improved if the slipping domain increases the inlet flow rate compared to the no-slip case. However, the slipping patch should not be located in the outlet region of the contact. These considerations are captured by the proposed expressions for $[x_{1,est.}, x_{2,est.}]$. It should nonetheless be noted that Eqs. 14-15 are based on several assumptions, i.e. a vanishing slip length, a separate derivation for $x_{1,est.}, x_{2,est.}$, and a link between flow and load changes established only for convergent gaps. This limits their generalization to more complex cases, for instance in presence of divergent gaps and the occurrence of cavitation. Still, Eqs. 14-15 provide a meaningful estimation for the location of the slipping patch in the monotonically convergent geometries which are the focus of this work. In fact, the values $[x_{1,est.}, x_{2,est.}]$ could be confirmed through a parametric study with small slip length ($b = 10^{-4}h_2$) for both the planar and circular sliders at all convergence ratios.

2.3. Theoretical gains in load support and friction reduction

The continuum equations from Section 2.1 are also used to asses theoretical improvements in load support and friction through the addition of the slipping domain. Figure 4 shows the dimensionless load carrying capacity for each optimum configuration as a function of different slip lengths and convergence ratios. In the no-slip geometry, the maximum load support is found for $a \simeq 2.2$, whereas parallel surfaces does not generate any pressure distribution.

However, significant improvements in hydrodynamic lift can be achieved through slip on parallel walls [10, 12]. Compared to the optimum no-slip configuration, load support can be doubled through high slip lengths, and gains of the order of 40% can be reached if $b = h_2$. When the slip length is smaller than the minimum surface gap, i.e. $b = 0.25h_2$, maximum hydrodynamic lift is obtained for slightly slanted surfaces, as both the slipping patch and the convergent geometry contribute to pressure generation. Here, a 10% improvement in load carrying capacity compared to the best no-slip case is obtained. Thus, improving load support through slip in the hydrodynamic regime ideally involves a modification of the contact geometry to parallel walls. In reality this may be impossible, for instance if surface tilting occurs under operation in MEMS. In this case, it is crucial to analyze improvements at a given convergence ratio between inlet and outlet film thickness. Figure 5 shows the change in hydrodyamic lift compared to the no-slip solution for each a value. At $h_1/h_2 = 1$ the theoretical gain tends towards infinity, since no pressure is generated by parallel surfaces. Improvements in load support are significant (more than 30%) up to $a = 2.5$. Then, possible gains drop rapidly for the planar slider at higher convergence ratios (Fig. 5a), reaching only a few percent at $a = 6.0$. Conversely, load support improvements for the circular slider remain of the order of 10% and above at all convergence ratios (Fig. 5b), if the slip length b is equal or larger than the film thickness h_2. In this case, introducing a slipping patch can still be considered as an effective way to achieve better hydrodynamic lift.

In addition to improving load support, slip can reduce friction at the same time. Fig. 6 shows the modification in the tangential friction force on the lower surface at a given convergence ratio a and as a function of the slip length. For parallel surfaces, a reduction in viscous losses up to 33% can be achieved. This is related to the lower shear rate of the lubricant due to added slip over a large domain of the contact length. However, theoretical improvements decrease rapidly with the convergence ratio for the planar slider (Fig. 6a), reaching only 2% at $a = 6.0$. In particular, the sharp loss in friction reduction for $a > 2.5$ is linked to the smaller size of the slipping patch, which at high surface slopes should not start at the contact inlet. Nonetheless, for the circular geometry (Fig. 6b) a decrease of viscous losses up to 10% is still possible at high a values if the condition $b \geq h_2$ is met.

In summary, the maximum improvements in both load support and friction are possible by re-engineering the contact geometry to flat surfaces. Our analysis reveals that adding slip on a planer slider with highly slanted walls does not give significant beneficial effects. However, if a curved geometry like a cylindrical tip is considered, moderate gains in contact performance are still possible even at high convergence ratios. Beneficial effects of slip are thus strongly dependent on the shape of the convergent, and oversimplifying the gap geometry can lead to underestimating possible gains in the hydrodynamic regime. In all cases, care should be taken to correctly position the slipping patch in accordance with the principles of Section 2.2. Furthermore, one should aim at achieving a slip length equal or larger than the minimum film thickness, i.e. $b \geq h_2$. This simple criterion will be used in the next section to discuss the effectiveness of different hydrophobic surfaces for improved load support in water-lubricated MEMS.

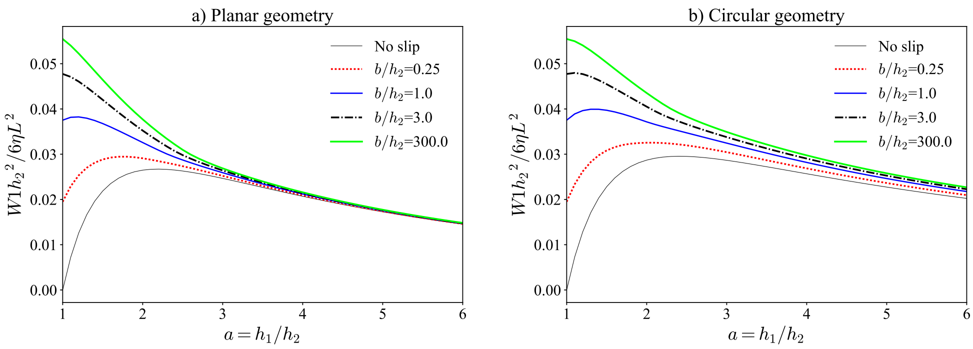

Figure 4: Dimensionless line load carrying capacity for the no-slip case and in presence of a slipping domain. For each slipping system the optimum configuration at a given convergence ratio a and slip length b is considered.

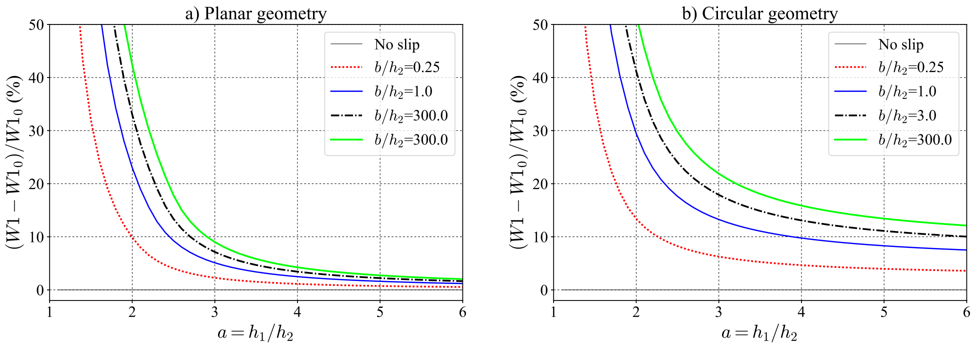

Figure 5: Relative change in hydrodynamic lift due to the slipping domain. Curves are obtained for the optimum slipping configuration at a given convergence ratio a and slip length b.

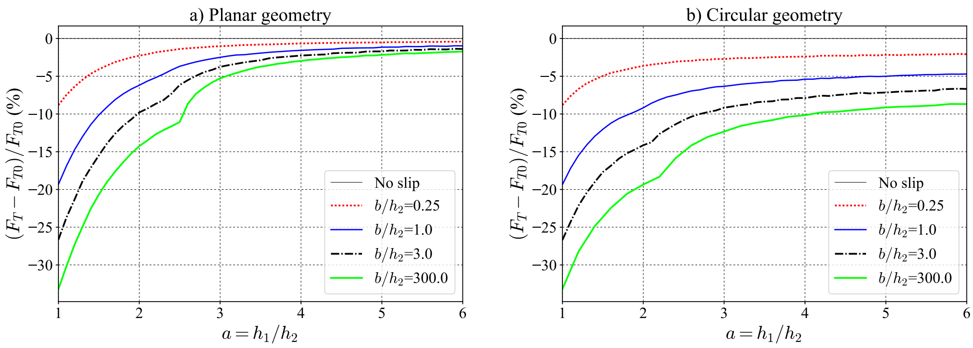

Figure 6: Relative change in friction force due to the slipping domain. Curves are obtained for the optimum slipping configuration at a given convergence ratio a and slip length b.

3. Slip length on hydrophobic surfaces and possible applications

In order to achieve the aforementioned improvements in load carrying capacity and friction, it is necessary to identify suitable materials and coatings capable of generating the desired slip boundary condition. For this purpose, Molecular Dynamics simulations provide a way to quantify wall slip on different surface topologies under tribological conditions and in nanometer-thin films expected in MEMS.

Which specific surface composition and chemistry leads to wall slip depends strongly on the fluid. The present work focuses on water, which constitutes an interesting alternative to traditional lubricants. This liquid is omnipresent in humid and biological environments, and is increasingly used as an operating fluid even in macroscopic mechanisms. Moreover, water is often found in contact spots between MEMS components due to capillary condensation.

At the atomic scale, wall slip is caused by weak wall-fluid interactions, low wall energy corrugation, or fluid-solid incommensurability. Hydrophobicity, high contact angles for water droplets on surfaces, or weak adsorption energies for single water molecules can be indicative of these properties. In the following, we will use Molecular Dynamics simulations as an exploratory tool for water on different kinds of hydrophobic surface topologies. The goal is to assess how much wall slip can occur under typical tribological conditions, and to discuss perspectives for the use of these surfaces in MEMS.

Two possible surfaces were identified in a study on polar hydrophobicity of fluorinated carbon compounds [19]. (111)-diamond surfaces with 100 % hydrogen terminations (Fig. 7a) are non-polar, resulting in weak electrostatic interactions and a small adsorption energy for water molecules. The nanoscopic contact angle of 60° is indicative of

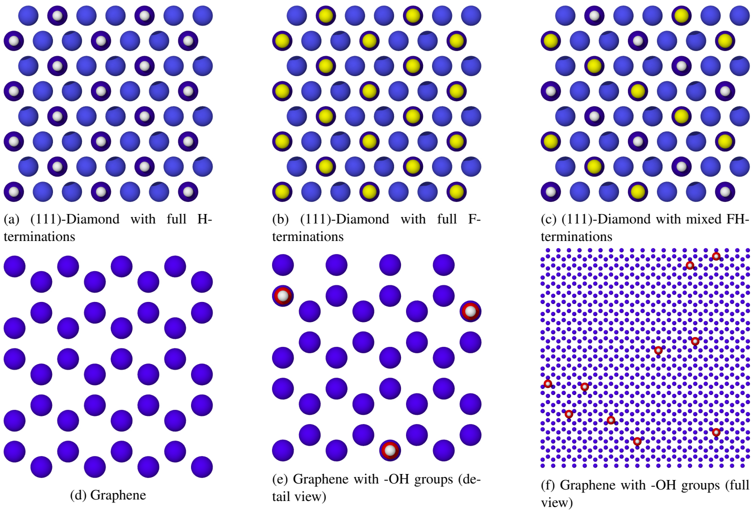

(a) (111)-Diamond with full H-terminations

(b) (111)-Diamond with full F-terminations

(c) (111)-Diamond with mixed FH-terminations

(d) Graphene

(e) Graphene with -OH groups (detail view)

(f) Graphene with -OH groups (full view)

Figure 7: Top view of the surfaces considered in this work. a-e represent patches of 1.0x1.0 nm^2, whereas (f) shows the position of OH groups in graphene oxides on a 4.92x5.11 nm^2 domain. Carbon atoms are displayed in blue, hydrogen in white, fluor in yellow, and oxygen in red.

moderate hydrophobicity. A similar behavior is obtained for fluor-terminated (111)-diamond (Fig. 7b). Despite the strong polarity of the C-F bonds, the resulting electric field decays very rapidly with surface distance and is not felt by the water molecules. This phenomenon, known as "polar hydrophobicity", leads to a small adsorption energy for water, and a nanoscopic contac angle of 80°. On the contrary, diamond surfaces with mixed FH-terminations (Fig. 7c) present stronger electrostatic interactions with water due to a slower decay of the electric field. This topology features a contact angle of 30°, and will be considered as representative of a hydrophilic case. It should be noted that the aforementioned surfaces feature an atomically smooth geometry which may be difficult to reproduce experimentally. Yet, assessing wall slip of water on such ideal surfaces constitutes a necessary step for the analysis more complex materials, like polymers or Self-Assembled-Monolayers.

Conversely, graphene layers (Fig. 7d) have often been produced and analyzed experimentally [29, 30]. In tribological applications, graphene coatings have been employed to reduce friction in dry conditions [31, 32]. Atomistic simulations have revealed that graphene nanotubes are extremely slippery for water, with application in membranes for enhanced fluid transport [33, 7]. These studies indicate the potential for graphene as a slipping surface in water-lubricated MEMS in the hydrodynamic regime. Finally, a graphene layer with additional hydroxyl (-OH) groups will also be considered (Fig. 7e-f). This topology is inspired from the graphene oxide surface in [34], one of the main precursors in the manufacturing process of graphene-based materials. The goal is to understand how side groups remaining from the production of graphene or stemming from tribochemical reactions may impact slip.

3.1. Molecular Dynamics simulations setup

Slip on the aforementioned surfaces is quantified using the Molecular Dynamics setup shown in Figure 8. Water is sheared in a nanometric gap between two walls of the same topology. The system dimensions are approximately 5.0 nm by 5.0 nm in width and length. Periodic boundary conditions are applied along the x- and y-directions. Three values are chosen for the film thickness (h = 10 nm, 5 nm, and 2.5 nm), with the respective systems containing approximately 5600, 2800 and 1400 water molecules. Shearing is imposed through the opposite movement of the surfaces at velocities $\pm U$ in $x-$direction. Values for the wall speed U range from 2 to 50 m/s.

Water is described through a standard TIP3P potential [18]. The surfaces are the five topologies from Fig. 7. For each (111)-diamond surface, 9 carbon layers and the terminations in contact with water are considered. The outermost surface layers are rigid (see Fig. 8) for the application of the operating conditions in load and shearing, while the rest of the structure is unconstrained. The atomic interactions are based on OPLS potential for hydrocarbons [35] and perfluoroalkanes [36]. Modifications are introduced in the bonded interactions for bulk diamond to reproduce its elastic constants, in the charge of C-F and C-H atoms, and in the Lennard-Jones σ for F and H to reproduce the

DFT adsorption energy for a single water molecule [19]. The graphene surface is constituted by a single rigid layer without substrate, representing the last atoms in direct contact with the fluid. The wall-fluid interactions are governed by a Lennard-Jones potential with $\epsilon_{OC} = 4.94 \cdot 10^{-3}$ eV and σ_{OC}=3.27 Å between carbon and oxygen atoms [33]. Similarly, a rigid carbon layer is considered for graphene with -OH groups, which are mobile. Atomic interactions are described by the OPLS potential for hydrocarbons [35].

MD calculations are performed in LAMMPS [37] with a time step of 1.0 fs. For each system, the operating conditions in terms of load and shearing are applied as follows. After a first equilibration of water, a pressure of 25 MPa is exerted on the walls until the film thickness h reaches a stable value. Note that other pressures ranging from 1 to 50 MPa were considered, but did not change results significantly under equilibrium and steady-state shearing. The vertical movement of the walls is then suppressed, and shearing is imposed through the velocities $+U$ and $-U$ to the rigid layers of the top and bottom surfaces. The fluid and the unconstrained layers of the surfaces are kept at a temperature of T=300 K by the means of a Nosé-Hoover thermostat coupled to the y-components only. This setup is sufficient to reach the target temperature in the system, and gives very similar results to thermostating both the $y-$ and $z-$directions under shearing. After steady-state is reached, the velocity profile of water across the gap is computed. Statistical averaging is carried out over 5-20 ns depending on the applied surface speed. The effective shear rate $\dot{\gamma}_{\text{eff}}$ is determined from the slope of the water velocity profile (see Fig. 9). Finally, the slip length is given by:

$$b = \frac{h}{2}\left(\frac{\dot{\gamma}_{\text{eff}} h}{2U} - 1\right) \tag{16}$$

The factor 2 arises from considering two surfaces with same topology in the MD simulation setup.

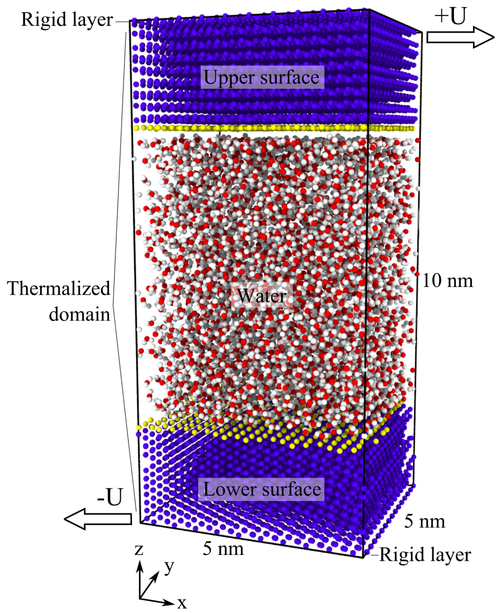

Figure 8: Snapshot of a typical Molecular Dynamics simulation setup for water between two hydrophobic surfaces. The configuration shown here is for (111)-diamond walls with 100% fluor terminations.

3.2. Results and discussion

Figure 9 shows the shear flow for the surface topologies from Fig. 7, a film thickness of h=5 nm and imposed surface velocities $\pm U$=20 m/s. A linear velocity profile across the gap width, i.e. a simple Couette shearing, is obtained in all cases. Slight deviations in direct proximity of the walls are linked to layering of the water molecules. In the center of the gap, nonlinearities in the velocity profiles are due to fluctuations and disappear if sampling is performed over longer simulation times in steady-state. These results are coherent with a hydrodynamic description of the fluid, allowing the slip length to be assessed through Eq. 16.

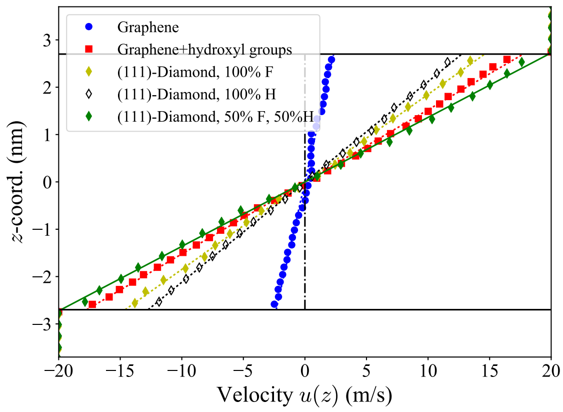

Figure 9: Velocity profiles of nanoconfined water sheared between two surfaces with topologies from Fig. 7. The film thickness is h=5.3 nm and the speeds imposed on the surfaces are ±20 m/s. The lines show the linear fit of the velocity profiles across the gap width.

Slip is negligible for water on (111)-diamond with mixed FH-terminations. This is due to the presence of electrostatic wall-fluid interactions, which account for the hydrophilic behavior of this surface. Conversely, all other wall topologies show some degree of slip under tribological conditions and in nano-confinement. A slip length of approximately 1 nm is found for fully H- and F- terminated (111)-diamond. In both cases, the interactions with water are mainly of dispersive nature, i.e. non-electrostatic. For the H-terminated surface, this is due to the weak charges of the hydrogen atoms. In the case of fluorinated diamond, the electric field generated by the narrowly spaced C-F dipoles decays rapidly with surface distance, and is not felt by the water molecules. However, fluor atoms present a deeper energy well of the Lennard-Jones potential compared to hydrogens, which can explain the slightly smaller slip length than for H-terminated (111)-diamond.

Compared to the previous wall topologies, graphene is a very slippery surface which entrains water very weakly. The slip length from our simulations is b=27 nm at T=300 K, which is in line with results from ab-initio Molecular Dynamics under equilibrium conditions [38]. However, the presence of 10 randomly distributed hydroxyl groups on the 5 nm x 5 nm graphene surface strongly suppresses the slip effect. A sub-nanometer slip length of only 0.3 nm is found in this case.

Additionally, a parametric study on the film thickness h and the surface velocity U has been performed. Results of Figure 10 show no significant variations of b with the applied shear rate ranging from $\dot{\gamma} = 5 \cdot 10^8$ Hz to $5 \cdot 10^{10}$ Hz, corresponding to a wide range of wall speeds and film thicknesses. Scattering of the values observed at lower shear rates is within the estimated error from the linear fit of the velocity profiles. The average value for the slip length of water on each surface is summarized in Table 1. It should be noted that the $\dot{\gamma}$ values considered in this study are much higher than those expected in typical microsystems. Molecular Dynamics simulations at shear rates relevant for MEMS would require prohibitive computational costs due to statistical averaging of the velocity profiles over much longer runs. Nonetheless, studies on slip dependence with the shear rate [39] and comparisons with equilibrium simulations [40] showed that for stiff walls the slip length remains constant below a critical value of $\dot{\gamma}$. Results of the present MD simulations can thus be considered valid at low shear rates found in MEMS, which justifies the use of a Navier boundary condition with fixed b in the continuum model. Finally, AFM experiments have been performed for water on highly ordered pyrolitic graphite and graphene oxide [41], which are similar to the graphene and hydroxilated graphene walls considered here: slip lengths of the same order of magnitude were reported, despite the significantly different operating conditions and surface geometry.

The continuum analysis indicates that the Navier slip length on the hydrophobic domain should be equal or larger than the film thickness, in order to achieve significant benefits in the hydrodynamic regime. Of all considered wall topologies, pure graphene is thus the most promising material for use in microsystems. This surface could be applied for full-film water films with thickness up to approximately 25 nm. On the other hand, other surface types considered in this work may prove beneficial for surface gaps at the nanometer or subnanometer level. This is representative of

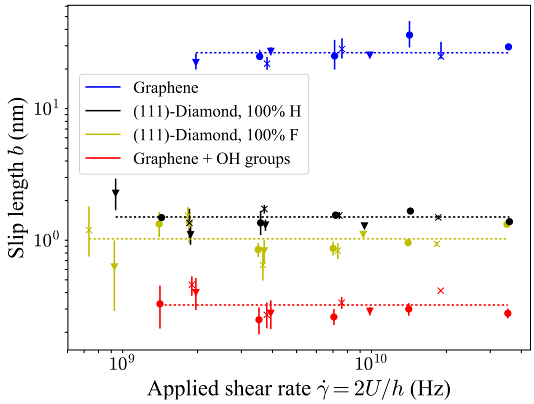

Figure 10: Slip lengths as a function of the applied shear rate $\dot{\gamma}$ for the surface topologies of Fig. 7. Circles mark a film thickness h=2.6 nm, crosses for h=5.3 nm, and triangles for h=10.6 nm. Dashed lines indicate the average slip length for each surface type. Each point corresponds to a single simulation, with the error bar associated to the linear fit of the shear velocity profile. Note that several runs for fully H-terminated diamond with h=5.3 nm, U=20 m/s indicated good repeatability of the results, whose spreading is well represented by the error bars shown here.

Surface	**Slip length (nm)**
(111)-diamond with mixed FH terminations	0
Graphene with OH groups	0.32 ± 0.06
(111)-diamond with full F terminations	1.02 ± 0.26
(111)-diamond with full H terminations	1.50 ± 0.27
Graphene	26.6 ± 3.9

Table 1: Average slip lengths for water at T=300K on the surface topologies of Fig. 7.

boundary lubrication, where contact between surfaces can occur and dominate the tribological processes of stiction and friction. A full understanding of this regime and potential benefits of slip requires extensions of the continuum model and further atomistic analysis to account for surface contact.

Nonetheless, the present work shows that hydrogenated or fluorinated carbon compounds can lead to reduced wall-fluid interactions with water. This opens up interesting perspectives for the analysis of Self Assembled Monolayers from fluorinated polymers. In this case, contact angles ranging from 120-190° can be observed [42], indicating high hydrophobicity and the possibility of achieving large slip. Further atomistic simulations could help assessing the slip length under tribological conditions and high confinement. Finally, future studies could focus on patterned surfaces with nanometer-sized ridges and pillars, which aim at achieving superhydrophobicity by mimicking the lotus effect found in nature [43]. Here, atomistic and continuum simulations can assist in the design of efficient geometrical nanopatterns. Additionally, further insight can be gained on the wetting of the nanostructures [44], and thus the resulting wall slip, under hydrodynamic pressures found under typical contact conditions.

4. Conclusion

This work discusses the addition of a slipping domain to a water-lubricated microsystem in the hydrodynamic regime, with the goal to assess possible gains in terms of load support and friction reduction. The problem is tackled using two complementary methods in a multiscale framework: a continuum hydrodynamics model and Molecular Dynamics simulations. On the one hand, the continuum analysis enables understanding how slip impacts tribological behavior at the scale of the contact length. Theoretical gains in hydrodynamic lift and friction can be assessed, allowing the formulation of simple criteria to discuss the effectiveness of different surface topologies in improving load support. On the other hand, Molecular Dynamics simulations provide quantitative information on slip occurring in nanometer-thin lubricant films found in microsystems. This can be used to justify the slip models used in the continuum equations, as well as to identify the surface topologies generating sufficient wall slip under tribological conditions.

The continuum hydrodynamics model is based on a flow analysis. A method for a convergent line contact is proposed to calculate pressure distribution modified by wall slip, as well the resulting load and friction, starting from the solution of the no-slip case. It is noteworthy that this method requires only the numerical evaluation of integrals. Using the continuum model, an extensive parametric study over the slip length and the convergence ratio of the contact geometry reveals that:

- For low surface slopes, the slipping region maximizing load support starts from the leading edge and extends approximately towards the middle of the contact. For high surface slopes, placing the slipping zone at the inlet has a negative effect on the load carrying capacity.
- To improve load support, the slipping domain should increase inlet flow rate, but should not be placed in the outlet region. These considerations allow the derivation of simple expressions for a quick estimation of its positioning, valid for the convergent geometries considered in this work.
- For large slip length, the maximum load carrying capacity is achieved with flat surfaces, and can be doubled compared to the optimum contact geometry without slip. For small slip the surface should be slightly slanted, since the convergent geometry also plays a role on pressure generation in the contact. Non-negligible gains in load support and friction can be still achieved for circular surfaces with high convergence ratios, if the slip length is of the same order or larger than the film thickness.

Molecular Dynamics simulations are then used to assess slip in nanometer-thin water films under tribological conditions for different hydrophobic surfaces, such as fluorinated or hydrogenated diamond, graphene, and graphene oxide. It is found that:

- The slip length for water on all considered surfaces is constant and independent on the shear rate, justifying the use of a Navier slip boundary condition in the continuum analysis.
- The use of graphene as a slipping coating in water-lubricated systems up to film thicknesses of 25 nm would be most beneficial. Other surfaces considered in this work may bring advantages only for surface gaps of the order of a nanometer.

Future work should thus aim at identifying other surfaces featuring larger slip in presence of water. Possible candidates are hydrophobic fluorinated polymers, or nanopatterned surfaces designed to achieve lotus effect.

5. Acknowledgments

The authors gratefully acknowledge the computing time for project *hfr14* granted by the John von Neumann Institute for Computing (NIC) and provided on the supercomputer JURECA at Jülich Supercomputing Centre (JSC) [45]. Supporting calculations were performed on the computational resource ForHLR II funded by the Ministry of Science, Research and the Arts Baden-Württemberg and DFG ("Deutsche Forschungsgemeinschaft").

6. Bibliography

[1] N. Tas, T. Sonnenberg, H. Jansen, R. Legtenberg, M. Elwenspoek, Stiction in surface micromachining, J. Micromechanics Microengineering 6 (4) (1996) 385–397. doi:10.1088/0960-1317/6/4/005.
[2] Z. Yapu, Stiction and anti-stiction in MEMS and NEMS, Acta Mech. Sin. 19 (l) (2003) 1–10. doi:10.1007/BF02487448.
[3] B. Smith, J. Sniegowski, G. LaVigne, Thin Teflon-like films for eliminating adhesion in released polysilicon microstructures, Proc. Int. Solid State Sensors Actuators Conf. (Transducers '97) 1 (1997) 159–163. doi:10.1109/SENSOR.1997.613629.
[4] W. R. Ashurst, C. Carraro, R. Maboudian, Vapor phase anti-stiction coatings for MEMS, IEEE Trans. Device Mater. Reliab. 3 (4) (2003) 173–178. doi:10.1109/TDMR.2003.821540.
[5] C. Navier, Mémoire sur les lois du mouvement des fluides, Mémoires lAcadémie R. des Sci. lInstitut Fr. VI (1823) 389–440.
[6] L. Bocquet, E. Charlaix, Nanofluidics, from bulk to interfaces, Chem. Soc. Rev. 39 (3) (2010) 1073–1095.
[7] K. Falk, F. Sedlmeier, L. Joly, R. R. Netz, Ultra-low liquid / solid friction in carbon nanotubes : comprehensive theory for alcohols , alkanes , OMCTS and water, Langmu 28 (40) (2012) 14261–14272.
[8] H. A. Spikes, The half-wetted bearing. Part 1: extended Reynolds equation, Proc. IMechE Part J J. Eng. Tribol. 217 (2003) 1–14.
[9] R. F. Salant, A. E. Fortier, Numerical Analysis of a Slider Bearing with a Heterogeneous Slip / No-Slip Surface, Tribol. Trans. 47 (2004) 328–334. doi:10.1080/05698190490455348.
[10] C. W. Wu, G. J. Ma, P. Zhou, C. D. Wu, Low Friction and High Load Support Capacity of Slider Bearing With a Mixed Slip Surface, J. Tribol. 128 (4) (2006) 904–907.
[11] A. Fatu, P. Maspeyrot, M. Hajjam, Wall slip effects in (elasto) hydrodynamic journal bearings, Tribol. Int. 44 (7-8) (2011) 868–877. doi:10.1016/j.triboint.2011.03.003.
[12] M. Tauviqirrahman, R. Ismail, J. Jamari, D. J. Schipper, A study of surface texturing and boundary slip on improving the load support of lubricated parallel sliding contacts, Acta Mech. 224 (2) (2013) 365–381. doi:10.1007/s00707-012-0752-7.
[13] M. Tauviqirrahman, R. Ismail, Jamari, D. J. Schipper, Optimization of the complex slip surface and its effect on the hydrodynamic performance of two-dimensional lubricated contacts, Comput. Fluids 79 (2013) 27–43. doi:10.1016/j.compfluid.2013.02.021.
[14] G. Bayada, M.-H. Meurisse, Impact of the cavitation model on the theoretical performance of heterogeneous slip/no-slip engineered contacts in hydrodynamic conditions, Proc. IMechE Part J J. Eng. Tribol. 3 (2009) 371–381.
[15] J.-T. Cheng, N. Giordano, Fluid flow through nanometer-scale channels, Phys. Rev. E 65 (2002) 31206.
[16] A. Ponjavic, M. Chennaoui, J. S. S. Wong, Through-Thickness Velocity Profile Measurements in an Elastohydrodynamic Contact, Tribol. Lett. 50 (2) (2013) 261–277.
[17] A. Ponjavic, J. S. S. Wong, The effect of boundary slip on elastohydrodynamic lubrication, RSC Adv. 4 (2014) 20821–20829.
[18] W. L. Jorgensen, J. Chandrasekhar, J. D. Madura, R. W. Impey, M. L. Klein, Comparison of simple potential functions for simulating liquid water, J. Chem. Phys. 79 (2) (1983) 926–935. doi:10.1063/1.445869.
[19] L. Mayrhofer, G. Moras, N. Mulakaluri, S. Rajagopalan, P. A. Stevens, M. Moseler, Fluorine-Terminated Diamond Surfaces as Dense Dipole Lattices: The Electrostatic Origin of Polar Hydrophobicity, J. Am. Chem. Soc. 138 (12) (2016) 4018–4028. doi:10.1021/jacs.5b04073.
[20] A. Martini, H. Y. Hsu, N. A. Patankar, S. Lichter, Slip at High Shear Rates, Phys. Rev. Lett. 100 (206001) (2008) 1–4. doi:10.1103/PhysRevLett.100.206001.
[21] A. Martini, A. Roxin, R. Q. Snurr, Q. Wang, S. Lichter, Molecular Mechanisms of Liquid Slip, J. Fluid Mech. 600 (2008) 257–269. doi:10.1017/S0022112008000475.
[22] N. Fillot, H. Berro, P. Vergne, From Continuous to Molecular Scale in Modelling Elastohydrodynamic Lubrication: Nanoscale Surface Slip Effects on Film Thickness and Friction, Tribol. Lett. 43 (2011) 257â266.
[23] A. Jabbarzadeh, R. I. Tanner, Thin lubricant films confined between crystalline surfaces: Gold versus mica, Tribol. Int. 44 (2011) 711–719. doi:DOI: 10.1016/j.triboint.2010.01.014.
[24] A. Vadakkepatt, Y. Dong, S. Lichter, A. Martini, Effect of molecular structure on liquid slip, Phys. Rev. E 84 (2011) 66311.
[25] D. Savio, N. Fillot, P. Vergne, M. Zaccheddu, A model for wall slip prediction of confined n-alkanes: Effect of wall-fluid interaction versus fluid resistance, Tribol. Lett. 46 (1) (2012) 11–22. doi:10.1007/s11249-011-9911-6.
[26] D. M. Huang, C. Sendner, D. Horinek, R. R. Netz, L. Bocquet, Water slippage versus contact angle: A quasiuniversal relationship, Phys. Rev. Lett. 101 (22) (2008) 226101.
[27] D. Savio, N. Fillot, P. Vergne, H. Hetzler, W. Seemann, G. E. M. Espejel, A Multiscale Study on the Wall Slip Effect in a Ceramic-Steel Contact With Nanometer-Thick Lubricant Film by a Nano-to-Elastohydrodynamic Lubrication Approach, J. Tribol. 137 (3) (2015) 31502.
[28] D. Savio, L. Pastewka, P. Gumbsch, Boundary lubrication of heterogeneous surfaces and the onset of cavitation in frictional contacts, Sci. Adv. 2 (3) (2016) e1501585–e1501585. doi:10.1126/sciadv.1501585.
[29] A. Geim, K. Novoselov, The rise of graphene, Nat. Mater. 6 (2007) 183–191. doi:10.1038/nmat1849.

[30] S. Kawai, A. Benassi, E. Gnecco, H. Sode, R. Pawlak, X. Feng, K. Mullen, D. Passerone, C. A. Pignedoli, P. Ruffieux, R. Fasel, E. Meyer, Superlubricity of graphene nanoribbons on gold surfaces, Science (80-.). 351 (6276) (2016) 957–961. doi:10.1126/science.aad3569.
[31] D. Marchetto, C. Held, F. Hausen, F. Wählisch, M. Dienwiebel, R. Bennewitz, Friction and wear on single-layer epitaxial graphene in multi-asperity contacts, Tribol. Lett. 48 (1) (2012) 77–82. doi:10.1007/s11249-012-9945-4.
[32] D. Berman, A. Erdemir, A. V. Sumant, Reduced wear and friction enabled by graphene layers on sliding steel surfaces in dry nitrogen, Carbon N. Y. 59 (2013) 167–175. doi:10.1016/j.carbon.2013.03.006.
[33] K. Falk, F. Sedlmeier, L. Joly, R. R. Netz, L. Bocquet, Molecular Origin of Fast Water Transport in Carbon Nanotube Membranes: Superlubricity versus Curvature Dependent Friction, Nano Lett. 10 (2010) 4067.
[34] W. Gao, L. B. Alemany, L. Ci, P. M. Ajayan, New insights into the structure and reduction of graphite oxide, Nat. Chem. 1 (5) (2009) 403–408. doi:10.1038/nchem.281.
[35] W. L. Jorgensen, D. S. Maxwell, J. Tirado-rives, Development and Testing of the OPLS All-Atom Force Field on Conformational Energetics and Properties of Organic Liquids, J. Am. Chem. Soc 118 (15) (1996) 11225–11236.
[36] E. K. Watkins, W. L. Jorgensen, Perfluoroalkanes: Conformational Analysis and Liquid-State Properties from ab Initio and Monte Carlo Calculations, J. Phys. Chem. A 105 (16) (2001) 4118–4125. doi:10.1021/jp004071w.
[37] S. Plimpton, Fast Parallel Algorithms for Short Range Molecular Dynamics, J. Comput. Phys. 117 (June 1994) (1995) 1–19. doi:10.1006/jcph.1995.1039.
[38] G. Tocci, L. Joly, A. Michaelides, Friction of water on graphene and hexagonal boron nitride from Ab initio methods: Very different slippage despite very similar interface structures, Nano Lett. 14 (12) (2014) 6872–6877. doi:10.1021/nl502837d.
[39] P. A. Thompson, S. M. Troian, A general boundary condition for liquid flow at solid surfaces, Nature 389 (1997) 360–362.
[40] S. K. Kannam, B. D. Todd, J. S. Hansen, P. J. Daivis, Slip flow in graphene nanochannels, J. Chem. Phys. 135 (14). doi:10.1063/1.3648049.
[41] D. Ortiz-Young, H.-C. Chiu, S. Kim, K. Voïtchovsky, E. Riedo, The interplay between apparent viscosity and wettability in nanoconfined water, Nat. Commun. 4. doi:10.1038/ncomms3482.
[42] J. Zhang, J. Li, Y. Han, Superhydrophobic PTFE Surfaces by Extension, Macromol. Rapid Commun. 25 (11) (2004) 1105–1108. doi:10.1002/marc.200400065.
[43] B. Bhushan, Y. C. Jung, K. Koch, Micro-, nano- and hierarchical structures for superhydrophobicity, self-cleaning and low adhesion, Philos. Trans. R. Soc. A Math. Phys. Eng. Sci. 367 (1894) (2009) 1631–1672. arXiv:arXiv:1011.1669v3, doi:10.1098/rsta.2009.0014.
[44] C. Cottin-Bizonne, J.-L. Barrat, L. Bocquet, E. Charlaix, Low-friction flows of liquid at nanopatterned interfaces, Nat. Mater. 2 (2003) 237–240.
[45] D. Krause, P. Thörnig, JURECA: General-purpose supercomputer at Jülich Supercomputing Centre, J. large-scale Res. Facil. JLSRF 2 (0) (2016) A62. doi:10.17815/jlsrf-2-121.

7. Appendix A

This Section aims at providing an estimation for the upper limit $x_{2,est.}$ of the slipping patch which maximizes load support. For this purpose the relationship between flow rate and load support for slip at the contact outlet should be analyzed further. In fact, results from Section 2.2 indicate that slip should enhance fluid flow to improve contact performance. Yet, if the slipping domain is located at the exit, a severe loss in hydrodynamic lift is found despite maximizing the flow rate (Figure 2).

We start with the system configuration from Figure 1, where the domain with constant Navier slip length b extends between abscissas x_1 and x_2 (Eq.3). The pressure distribution $P(x)$ from Eq. 11 can be decomposed into three zones:

$$P(x) = \begin{cases} \int_0^x \frac{\partial P_0}{\partial x} dx - 12\eta \int_0^x h^{-3} dx, & \text{if } x < x_1. \\ P(x_1) + \int_{x_1}^x \left[\frac{\partial P_0}{\partial x} \left(\frac{b+h}{4b+h} \right) + \frac{6\eta U}{h^2} \left(\frac{b}{4b+h} \right) \right] dx - 12\eta \int_{x_1}^x \left[\frac{b+h}{h^3(4b+h)} \right] dx, & \text{if } x_1 < x < x_2. \\ P(x_2) + \int_{x_2}^x \frac{\partial P_0}{\partial x} dx - 12\eta \int_{x_2}^x h^{-3} dx, & \text{if } x > x_2. \end{cases} \quad (17)$$

Note that $P(x_1)$ and $P(x_2)$ are obtained from the integral expressions in the previous domains. We now extend the slipping patch by a small amount δ towards the outlet. This introduces an additional modification $\delta\Phi$ in fluid flow and $\delta P(x)$ in the pressure distribution.

Similar to Eq. 17, one can express the new pressure distribution $P(x)+\delta P(x)$ over the four domains $[0, x_1]$, $[x_1, x_2]$,

$[x_2, x_2 + \delta]$, $[x_2 + \delta, L]$. Subtracting $P(x)$ gives:

$$\delta P(x) = \{ \begin{array}{ll} -12\eta\delta \int_{0}^{x} h^{-3} dx, & \text{if} x < x_1. \\ -12\eta\delta \left[\int_0^{x_1} h^{-3} dx + \int_{x_1}^{x} \left[\frac{b+h}{h^3(4b+h)} \right] dx \right], & \text{if } x_1 < x < x_2. \\ \delta P(x_2) - 12\eta(+\delta) \int_{x_2}^{x} \left[\frac{b+h}{h^3(4b+h)} \right] dx + 12\eta \int_{x_2}^{x} h^{-3} dx & \\ + \int_{x_2}^{x} \left[\frac{\partial P_0}{\partial x} \left(\frac{-3b}{4b+h} \right) + \frac{6\eta U}{h^2} \left(\frac{b}{4b+h} \right) \right] dx, & \text{if } x_2 < x < x_2 + \delta. \\ \delta P(x_2 + \delta) - 12\eta\delta \int_{x_2+\delta}^{x} h^{-3} dx, & \text{if } x > x_2 + \delta. \end{array} \tag{18}$$

Pressure is imposed at the outlet of the contact $x = L$, leading to $\delta P(L) = 0$ and consequently $\delta P(x_2 + \delta) = 12\eta\delta\Phi \int_{x_2+\delta}^{L} h^{-3} dx$. The last term in Equation 18 can thus be rewritten as $12\eta\delta\Phi[\int_{x_2+\delta}^{L} h^{-3} dx - \int_{x_2+\delta}^{x} h^{-3} dx]$. Adding and subtracting $12\eta\delta\Phi \int_0^{x_2+\delta} h^{-3} dx$ to this expression, and regrouping the integrals finally gives $\delta P(x > x_2 + \delta) = 12\eta\delta\Phi[\int_0^{L} h^{-3} dx - \int_0^{x} h^{-3} dx]$.

We shall now focus on pressure changes δP outside the added slipping domain $[x_2, x_2 + \delta]$, due to its negligible dimensions compared to the contact length. Assuming a vanishing slip length ($b \to 0$) the first two terms of Equation 18 can be simplified and grouped together, giving:

$$\delta P(x) = \begin{cases} -12\eta\delta\Phi \int_0^{x} h^{-3} dx, & \text{if } x < x_2. \\ 12\eta\delta\Phi \left[\int_0^{L} h^{-3} dx - \int_0^{x} h^{-3} dx \right], & \text{if } x > x_2 + \delta. \end{cases} \tag{19}$$

In the following we assume the flow rate change $\delta\Phi$ due to the extension of the slipping patch to be positive. In fact, Figure 2b indicates that slip further increases fluid flow if extended in the middle and outlet regions (cf. the blue domain). Note nonetheless that this flow consideration is obtained for convergent geometries in Section 2.2, and that generalization to other cases may be limited. As $\delta\Phi > 0$, the sign of the integral terms in Eq. 19 determines whether the pressure distribution along the contact length is increased or decreased by the extension. Eq. 19 starts with the boundary condition $\delta P(x = 0) = 0$, and is negative in the $[0, x_2]$ region. After abscissa $x_2 + \delta$, Eq. 19 follows a second curve, shifted by a constant $12\eta\delta\Phi \int_0^{L} h^{-3} dx$ to comply with the boundary condition $\delta P(x = L) = 0$ at the contact outlet. In this domain δP is positive. The transition between the two curves occurs in the added slip domain $[x_2, x_2 + \delta]$, which is of negligible size compared to the contact length and will be neglected in the following. In summary, extending the slipping patch introduces both a negative and a positive contribution to the pressure field along the whole contact length, respectively for $x < x_2$ and $x > x2 + \delta$. Their magnitude depends therefore on the location x_2.

Finally, integrating Eq. 19 along the contact length gives the change in load support $\delta W1$ due to the extension of the slipping domain:

$$\delta W1 = 12\eta\delta\Phi \left[-\int_{\zeta=0}^{L} \left(\int_{x=0}^{\zeta} h(x)^{-3} dx \right) d\zeta + (L - x_2) \int_0^{L} h(x)^{-3} dx \right] \tag{20}$$

$\delta W1$ is thus related to the product of two terms: the flow rate change $\delta\Phi$, and an additional contribution depending on the geometry $h(x)$ of the convergent, and the upper limit of the slipping domain x_2. This second term will be denoted from now on as $W_h(x_2) = \left[-\int_0^{L} \left(\int_0^{\zeta} h(x)^{-3} dx \right) d\zeta + (L - x_2) \int_0^{L} h(x)^{-3} dx \right]$. For $\delta\Phi > 0$, the sign of $W_h(x_2)$ determines if $\delta W1$ is positive or negative, and thus whether the extension of the slipping patch improves or reduces load support. In particular, $W_h(x_2)$ is a linear function of the upper bound x_2 of the slipping patch.

For low x_2, i.e. if the upper bound of the slipping domain is located in the inlet and middle regions, $W_h > 0$: here, an extension of the slipping patch improves load support. Conversely, W_h is negative for x_2 near the contact exit. As indicated by Eq. 19, the domain $x < x_2$ where pressure is reduced by the slip extension is large compared to the region $x > x_2 + \delta$ where δP is increased. Consequently, $\delta W1$ is also negative: a loss in load carrying capacity occurs even if the extension of the slipping patch enhances flow rate.

In summary, slip should not be extended beyond a certain abscissa along the contact length, which can be quantified as the crossover point $x_{2,est}$ where W_h and thus $\delta W1$ change from positive to negative:

$$x_{2,est} = L - \frac{\int_0^L \left[\int_0^\zeta h(x)^{-3} dx \right] d\zeta}{\int_0^L h(x)^{-3} dx} \tag{21}$$

This location marks the beginning of the outlet zone where adding slip causes losses in load support. Thus, it corresponds to our estimation for the upper limit of the optimum slipping patch.